



Boosting alkaline photocatalytic H₂O₂ generation by incorporating pyrophosphate on g-C₃N₄ for effective proton shuttle and oxygen activation

Liangpang Xu^b, Lejing Li^b, Zhuofeng Hu^{a,*}, Jimmy C. Yu^{b,*}

^a School of Environmental Science and Engineering, Guangdong Provincial Key Laboratory of Environmental Pollution Control and Remediation Technology, Sun Yat-sen University, Guangzhou 510275, China

^b Department of Chemistry, The Chinese University of Hong Kong, Shatin, New Territories, 999077, Hong Kong, China

ARTICLE INFO

Keywords:

Alkaline H₂O₂ production
Pyrophosphate-incorporated g-C₃N₄
Proton shuttle
Oxygen activation
Organic pollutant treatment

ABSTRACT

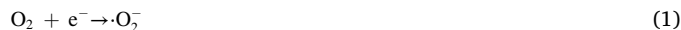
A novel pyrophosphate-based proton shuttle strategy has been proposed to boost on-site photocatalytic H₂O₂ generation in alkaline waters for organic pollutant treatment. Pyrophosphate-incorporated g-C₃N₄ (PCN) photocatalyst was prepared by facile thermal polymerization to address the issue of lack of protons in alkaline conditions. The PCN shows a record-high alkaline H₂O₂ synthesis rate (e.g. 1071.7 μmol g⁻¹ h⁻¹ at pH 9) under visible light together with an apparent quantum yield (Φ_{AQY}) of 8.7 % (at 420 nm). Mechanism study demonstrates that the pyrophosphate could serve as proton shuttle to effectively adsorb and provide protons, and act as advanced active sites for O₂ adsorption and activation to promote O₂ reduction, which greatly benefits the capture of nearby protons by the activated O₂ to form H₂O₂. This work provides a promising approach to prepare photocatalysts with superior alkaline H₂O₂ synthesis efficiency for on-site treatment of organic pollutants.

1. Introduction

Hydrogen peroxide (H₂O₂) is an effective and green oxidant which has been widely used for environmental treatment, typically in the advanced oxidation processes (AOPs) for degradation of organic pollutants [1,2]. The current industrial anthraquinone (AQ) method for H₂O₂ synthesis, however, is energy-consuming and could cause severe environmental concerns [3]. Moreover, the product of high-concentration H₂O₂ solution (e.g. 30 wt. %) suffers from self-decomposition, and issues on cost and safety in the storage and transportation processes. Hence, it has been a topic of great interest to develop sustainable and green approaches for on-site H₂O₂ synthesis [4, 5].

H₂O₂ has critical applications in alkaline conditions, including removal of organic pollutants from polluted water and bleaching of textiles [6–8]. However, traditional methods are not optimized for on-site H₂O₂ synthesis in alkaline water. For example, the AQ method has to consume quantities of organics, and the electrochemical method requires electrolyte of high-concentration salts together with extra energy and equipment inputs [3,9]. Photocatalysis is a more promising approach for this purpose. Driven by solar energy, this method could produce H₂O₂ using ubiquitous O₂ and water through oxygen reduction

by photo-generated electrons (Eqs. 1–2 or Eq. 3) [10,11]. The metal-free g-C₃N₄ is usually considered a promising photocatalyst for H₂O₂ synthesis due to its unique features of good stability, easy-to-modify, appropriate band structure for visible light absorption and oxygen reduction [12–14]. Recently, new star materials have also attracted much attention, such as covalent organic frameworks (COFs) [15], transition metal sulfide [16], etc. However, both of them have specific limitations restricting their large-scale utilizations: the synthesis of high crystallinity COFs is complicated and time-consuming, and the recycling stability of COFs is strictly limited by their poor moisture tolerance [17]; the transition metal sulfide usually suffers from poor reusability due to corrosion and leaching of metals [18,19]. Moreover, photocatalysis is an effective approach for H₂O₂ activation to generate hydroxyl radicals (·OH) (Eq. 4), a strong and widely used oxidative species [20,21]. The simultaneous occurrence of photocatalytic H₂O₂ generation and activation would provide opportunities for sustainable and convenient on-site treatment of pollutants.



* Corresponding authors.

E-mail addresses: huzhf8@mail.sysu.edu.cn (Z. Hu), jimyu@cuhk.edu.hk (J.C. Yu).

<https://doi.org/10.1016/j.apcatb.2023.122490>

Received 8 December 2022; Received in revised form 28 January 2023; Accepted 18 February 2023

Available online 21 February 2023

0926-3373/© 2023 Elsevier B.V. All rights reserved.



Nevertheless, alkaline photocatalytic H_2O_2 synthesis is challenging due to the limited supply of protons from a sluggish water dissociation. Proton is one of the key reactants for H_2O_2 generation in either the two-step (Eqs. 1–2) or one-step (Eq. 3) oxygen reduction reaction (ORR) [10]. In previous studies, acidic conditions (pH as low as 1–3) are often required for photocatalytic H_2O_2 synthesis [5,22–24], which proceeds easily by consuming the existing protons in acidic water. However, in alkaline conditions, the reaction kinetics of proton-consuming reactions would be significantly inhibited [25,26]. For example, the reaction kinetics of alkaline electrocatalytic hydrogen evolution reaction (HER) is two to three orders of magnitude slower than that of acidic HER [25]. To date, only a few studies have reported photocatalytic H_2O_2 generation in alkaline conditions [27,28]. However, they either rely on hole sacrificial agents (e.g. 5 vol. % ethanol), or suffer from limited efficiency for H_2O_2 synthesis ($< 0.49 \text{ mmol g}_{\text{cat}}^{-1} \text{ h}^{-1}$ at pH 9). A more ideal strategy to realize alkaline H_2O_2 synthesis is the fabrication of advanced photocatalysts for more efficient water dissociation and proton adsorption.

Incorporation of functional molecules with proton shuttle capacity on photocatalysts should potentially benefit alkaline H_2O_2 generation. The pyrophosphate is a good candidate for this purpose. With four pK_a values (i.e. 0.9, 2.0, 6.6, 9.4), the pyrophosphate owns strong proton shuttle property and is thus a good buffering agent even in pH 12 [29]. The multiple Lewis basic $[\text{P-O}]^-$ groups of pyrophosphate could obtain protons from water to form $[\text{P-OH}]$, which exhibits a much higher dissociation constant (K_d) than that of water. For example, at pH 9.4, the K_d for $[\text{HP}_2\text{O}_7]^{3-}/[\text{P}_2\text{O}_7]^{4-}$ is $10^{-9.4}$, more than four orders of magnitude higher than that of water (10^{-14}). In this case, the pyrophosphate could effectively provide protons for proton-consuming ORR even in alkaline water. Furthermore, given the well-known role of Lewis acid or Lewis basic groups as active sites to promote chemical reactions [30], the abundant Lewis basic $[\text{P-O}]^-$ groups as electron-rich center may also serve as active sites to facilitate adsorption and reduction of electrophilic O_2 molecules [31].

Here, we report efficient alkaline photocatalytic H_2O_2 generation on pyrophosphate-incorporated $\text{g-C}_3\text{N}_4$ (PCN) for on-site treatment of organic pollutants. The PCN could produce H_2O_2 in a rate of $1071.7 \mu\text{mol g}_{\text{cat}}^{-1} \text{ h}^{-1}$ at pH 9 under visible light, exceeding that of the state-of-the-art alkaline ORR photocatalysts. Through experimental and theoretical studies, it was found that the pyrophosphate on PCN plays multiple critical roles: 1) proton shuttle to effectively provide protons for H_2O_2 generation, 2) advanced active sites for O_2 reduction, and 3) boosting the charge separation and transfer of PCN. Furthermore, taking the advantage of photocatalysis for H_2O_2 activation, the H_2O_2 product could fulfill in-situ application for efficient treatment of various kinds of organic pollutants. This work provides a novel strategy to achieve alkaline H_2O_2 production for on-site environmental treatment.

2. Experimental section

2.1. Synthesis of catalyst

The preparation of $\text{g-C}_3\text{N}_4$ catalysts is through a classic thermal treatment. Specifically, pyrophosphate-incorporated $\text{g-C}_3\text{N}_4$ (PCN) was prepared with 1.5 g melamine and different quantities of sodium pyrophosphate ($\text{Na}_4\text{P}_2\text{O}_7$) as precursors. They were thoroughly grinded and placed in a ceramic crucible, followed by calcination at 550°C for 4 h. The solid product was washed using water and ethanol and then dried in an oven. The catalysts prepared with 0.5, 0.75, and 1 g pyrophosphate were denoted as PCN1, PCN2, and PCN. Notably, with excess pyrophosphate (e.g. 1.5 g), no solid catalyst was obtained. Similarly, Na-doped $\text{g-C}_3\text{N}_4$ was prepared with 1.5 g melamine and 0.44, 0.66, or 0.88 g NaCl as precursors, which were denoted as NaCN1, NaCN2, and NaCN, respectively. Pristine $\text{g-C}_3\text{N}_4$ (CN) was prepared by using only melamine as precursor. The as-prepared catalysts were characterized by

a series of measurements to show their morphologies, chemical states, and other natures (see details in Supporting Information Text S1).

2.2. Photocatalytic production of H_2O_2

In a typical photocatalytic reaction, 10 mg catalyst was added into 50 ml deionized water. The suspension was subjected to ultrasonication for 20 min. The pH was adjusted to specific value using 0.1 M KOH and H_2SO_4 . For production of H_2O_2 , bubbling with O_2 at a flow rate of 0.3 L/min was involved to make the suspension saturated with O_2 . Then, the suspension was irradiated by a 300 W Xenon lamp (Perfectlight, China), and a 420 nm cutoff filter was equipped to the lamp to cut UV light. The photo-reactor is cylindrical, and the diameter is 5.5 cm, the thickness for reaction solution (50 ml) is 3.6 cm. During the photoreaction, the temperature of the suspension was kept at 25°C by a water-circulating system. At designed time intervals, the sample of suspension was taken out for analysis after centrifugation. The concentration of H_2O_2 was determined by a I_3^- method described in our previous report [32].

2.3. Photocatalytic degradation of organic pollutants

The setup for degradation of pollutants is similar to that for production of H_2O_2 . Different kinds of pollutants (initially at $50 \mu\text{M}$), including bisphenol A (BPA), ofloxacin (OFL), or Rhodamine B (RhB), were added into the suspension of catalysts (0.2 g/L). The suspension was stirred for 30 min to reach sorption-desorption equilibrium, and then subjected to visible-light irradiation. The concentration of BPA and OFL were determined by high performance liquid chromatography (HPLC, Agilent 1260), and RhB was measured by a UV-vis spectrophotometer (Agilent Cary 100).

2.4. Photoelectrochemical measurements

The Mott-Schottky plots, polarization curves, and photocurrent responses were conducted using an electrochemical workstation (CHI 660D, CH Instrument, China). A typical three-electrode system was constructed. The reference electrode and counter electrode are saturated-KCl/AgCl and platinum foil ($1.0 \times 1.0 \text{ cm}^2$), respectively. The working electrode was fabricated by coating catalyst on a FTO glass ($1.0 \times 1.0 \text{ cm}^2$). The electrolyte was 0.1 M Na_2SO_4 solution.

2.5. Theoretical calculation

The calculations used the Vienna Ab initio Simulation Package (VASP). We applied projector-augmented-wave method with Perdew-Burke-Ernzerhof GGA functional. We set the electronic convergence limit at $1 \times 10^{-4} \text{ eV}$. The optimization of atomic coordinates was taken as converged if Hellmann-Feynman force was smaller than $2 \times 10^{-2} \text{ eV \AA}^{-1}$. The slab consisted of $\text{g-C}_3\text{N}_4$ framework, an oxygen and pyrophosphate molecule are constructed. The vacuum region is about 15 \AA in height.

3. Results and discussion

3.1. Characterization of catalysts

Scanning electron microscope (SEM) and transmission electron microscope (TEM) images show the anisotropic sheet-like morphology of CN and PCN (Fig. S1). From atomic force microscope (AFM) images (Fig. S2), it could be clearly found that the PCN is sheet-like, different from the irregular particle of CN. Moreover, the thickness of PCN ($< 0.8 \text{ nm}$) is much smaller than that of CN ($< 9.9 \text{ nm}$). From the SEM energy dispersive spectroscopy (EDS) mapping images, the C, N, P, O, and Na were found to show uniform distributions in PCN (Fig. S3). The crystal and phase structure of PCN with incorporation of different content of pyrophosphate were investigated by XRD measurements. As

presented in Fig. 1a, two classic peaks at 13.4° and 27.3° attributed to (100) and (002) facets were observed for CN, representing the in-plane repeating of tri-s-triazine motifs and typical periodic graphitic stacking of the conjugated aromatic system, respectively [33,34]. With the incorporation of more pyrophosphate (CN < PCN1 < PCN2 < PCN), the (100) peak gradually vanishes, indicating the in-plane distortion of the heptazine units [5]. Besides, the (002) peak becomes broader and weaker, suggesting the inhibited stacking of aromatic system to form thinner particles [35]. The weaker XRD signal of PCN suggests the decrease of crystallinity induced by doping of Na and incorporation of pyrophosphate on g-C₃N₄. This effect could favor the activity of PCN by promoting visible-light absorption and charge transfer to catalyst's surfaces [36,37].

FT-IR and XPS measurements were conducted to investigate the chemical states of catalysts. Typical C-N heterocyclic structure was observed for CN, including the stretching vibration modes at 1158, 1247, 1328, 1415 cm⁻¹ for C-N, 1576 and 1642 cm⁻¹ for C=N, and 807 cm⁻¹ for characteristic breathing mode of triazine units (Fig. 1b) [35]. Moreover, the broad signal at ~ 3200 cm⁻¹ represents stretching vibrations of N-H/O-H. These signals are also observed for PCN, confirming the remaining of C-N heterocyclic structure. However, due to the incorporation of pyrophosphate, the signals of O-P were observed at 994 and 931 cm⁻¹ [38]. The peaks at 1160 and 1119 cm⁻¹ are breathing modes of C-O [39], indicating the binding of g-C₃N₄ with pyrophosphate via formation of C-O bonding. Furthermore, the signal of cyano groups (C≡N) at 2170 cm⁻¹ transformed from the terminal -C-NH₂ is much stronger for PCN [40,41]. The presence of more cyano groups on PCN could contribute to a higher photocatalytic performance by enhancing visible-light absorption, charge separation and transfer [41,42].

According to XPS survey spectra (Fig. S4a), besides the C, N, and O observed in CN, P and Na are also found in PCN. The atomic ratios of CN and PCN are shown in Table S1. Compared with CN, the content of P and O for PCN increase by 2.5 % and 10 %, respectively. The increased ratio of P to O is 1:4, close to the original composition of pyrophosphate (P₂O₇⁴⁻, 1:3.5). This observation suggests the incorporation of pyrophosphate on PCN, instead of P-doping. Moreover, loss of N also occurs for PCN as indicated from the decreased ratio of N (Table S1), which could be attributed to the substitution of N by O from pyrophosphate.

The signals corresponding to N-C=N, C-NH_x/C≡N, and C-C/C=C in C 1 s spectrum, together with bicoordinated N atoms (C=N-C), tertiary nitrogen atoms/cyano groups (N₃C/N≡C), and terminal amino groups (N-H_x) in N 1 s spectrum, are observed for PCN (Fig. 1c, Fig. S4b). This is similar to that of CN, indicating the remained C-N heterocyclic structure of PCN (Figs. S4c-4d). In addition, an extra peak at 289.2 eV was found for PCN, which corresponds well with previous reported C-O bond in g-C₃N₄ (288.9–289.1 eV) [40,43]. This suggests the binding of g-C₃N₄ with pyrophosphate via C-O bonding.

As shown in the O 1 s spectrum (Fig. 1d), the peaks of P-O-P (533.3 eV), O-P/O-H (532.2 eV), and C-O (530.8 eV) were observed for PCN [38,44], while there is only O-H for CN (Fig. S4e). This result further confirms the bonding of pyrophosphate with g-C₃N₄ by C-O bonding. The peak at 535.4 eV is assigned to the Na KLL spectrum [39]. Due to the use of sodium pyrophosphate as precursor, Na is also doped into the PCN. The Na 1 s binding energy at 1071.7 eV corresponds well to that of NaN₃ (Fig. S4f), suggesting the coordination of Na⁺ with in-planar N of PCN [45]. The P 2p spectrum of PCN could be divided into P1/2 and P3/2, corresponding to that of pyrophosphate (Fig. 1e) [46]. Notably, no other peak like P-C/P-N was found, implying the absence of direct bonding of P to PCN. From the ³¹P solid-state NMR spectrum (Fig. 1f), the signals centred at around 10 to 10 ppm can be assigned to pyrophosphate [47,48], further suggesting the remaining of pyrophosphate in PCN.

3.2. Band structure

The band structure of catalysts were investigated by a series of measurements. UV-vis diffuse reflectance spectroscopy (DRS) reveals the optical properties of materials. As shown in Fig. 2a, PCN shows a bright yellow color, which is deeper than that of CN (light yellow). It was found that PCN exhibits a stronger light absorbance compared with CN in the wavelength range of 300–800 nm. Moreover, the light absorption edge for PCN is extended to 500 nm, which is about 450 nm for CN. In this case, the PCN could make use of visible light with a longer wavelength and own a higher utilization efficiency of light. The band gap was determined by converting the UV-vis DRS to Tauc plots. Results show that PCN has a narrower band gap (2.68 eV) than that of CN (2.76 eV)

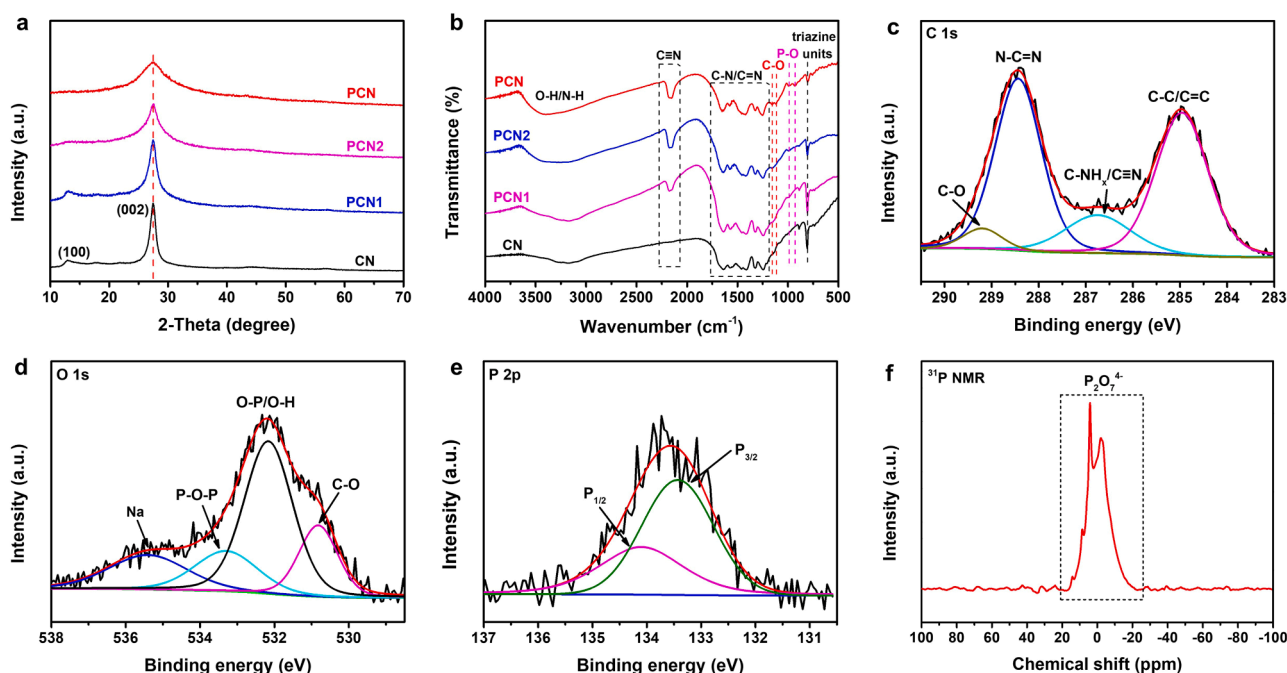


Fig. 1. (a) XRD patterns, and (b) FT-IR spectra of pristine g-C₃N₄ (CN) and pyrophosphate-incorporated g-C₃N₄ (PCN1, PCN2, and PCN). High-resolution (c) C 1 s, (d) O 1 s, and (e) P 2p spectra of PCN. (f) ³¹P solid-state NMR spectrum of PCN.

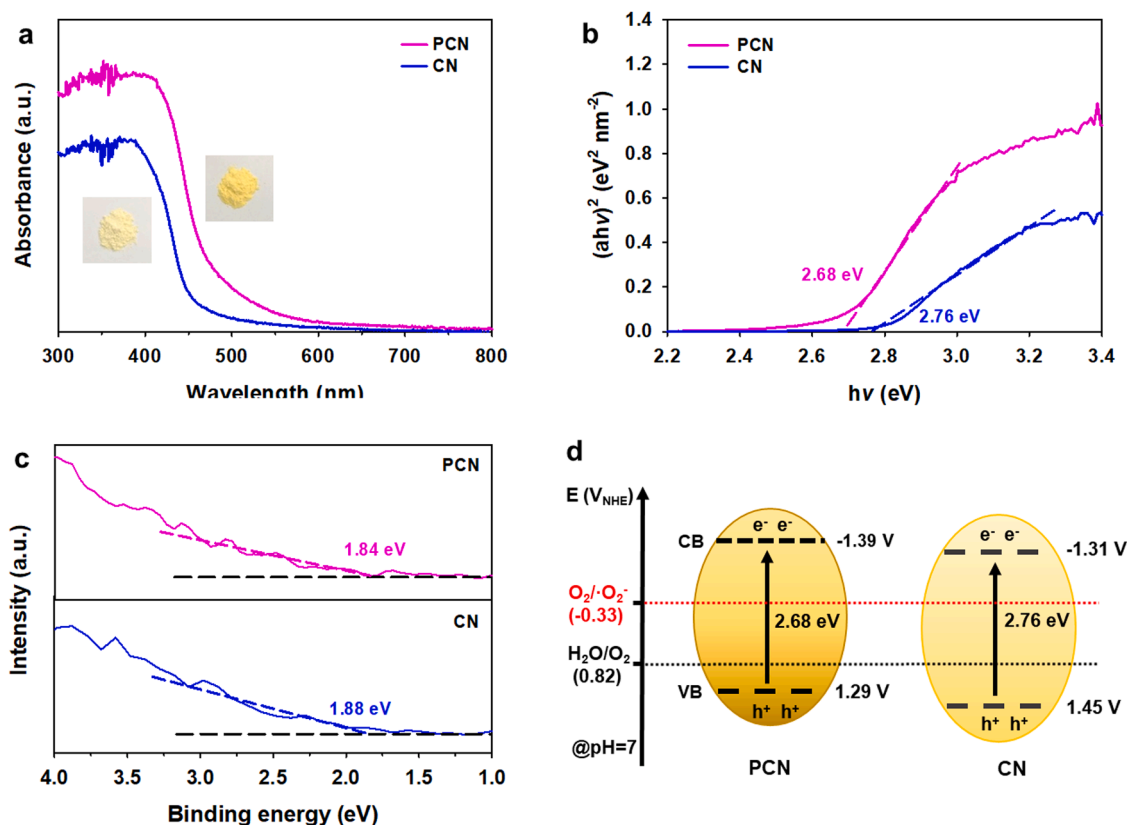


Fig. 2. (a) UV-vis diffuse reflectance spectra, (b) Converted Tauc plots, (c) Valence band XPS spectra, and (d) Band diagrams of PCN of CN.

(Fig. 2b).

The potential of conduction band (CB) and valence band (VB) were further determined by measurements of Mott-Schottky plots and VB XPS spectra. The flat-band potential was acquired from the x intercept of linear region in Mott-Schottky plots at a series of different frequencies [49,50]. As n-type semiconductor, the flat-band potential of g-C₃N₄ is close to the Fermi level [51]. Hence, it is reasonable to consider that the Fermi level of g-C₃N₄ is approximately equal to the flatband potential. Accordingly, the E_F for PCN and CN are -0.55 and -0.43 V (vs NHE), respectively (Fig. S5). Similarly, the VB potential (E_{VB}) of PCN and CN were found to be 1.84 and 1.88 V below their E_F (Fig. 2c). Accordingly, the E_{VB} were determined to be 1.29 V for PCN and 1.45 V for CN. The CB potential (E_{CB}) obtained by E_{VB} minus E_g was determined to be -1.39 and -1.3 V for PCN and CN, respectively. The band diagrams of the catalysts are shown in Fig. 2d. The negative shift of E_{CB} for PCN would be favorable for oxygen reduction to H₂O₂.

3.3. Photocatalytic production of H₂O₂

Photocatalytic production of H₂O₂ was investigated in weak alkaline condition (pH 8) under visible-light irradiation ($\lambda \geq 420$ nm). As shown in Fig. 3a, the H₂O₂ production rate for CN is negligible ($4.2 \mu\text{M h}^{-1}$). Nevertheless, with the incorporation of pyrophosphate, the activity was significantly improved. The H₂O₂ generation on PCN1, PCN2, and PCN reach 151.6 , 201.7 , and $254.3 \mu\text{M h}^{-1}$, respectively. Compared with CN, a remarkable enhancement as high as 61 times has been achieved for PCN. Furthermore, for catalysts with Na doping (NaCN) but without pyrophosphate, the H₂O₂ generation rate ($< 46.0 \mu\text{M h}^{-1}$) is much lower compared with PCN (Fig. S6). This result suggests the major role of pyrophosphate on efficient H₂O₂ generation in alkaline water, instead of Na-doping.

Given the great importance for environmental treatment, the production of H₂O₂ at different pH values (pH 5-10) were evaluated.

Despite of the gradual decrease with increasing pH, the H₂O₂ generation rate for PCN is still significant at pH 10 ($128.4 \mu\text{M h}^{-1}$), which is 41 times higher than that for CN ($3.2 \mu\text{M h}^{-1}$) (Fig. 3b). The efficient alkaline production of H₂O₂ on PCN could make it possible to proceed on-site environmental treatment. Moreover, the performance of PCN for alkaline H₂O₂ production also exceeds the state-of-the-art photocatalysts by two folds (Table S2), indicating the outstanding photocatalytic activity of PCN. The highest H₂O₂ yield for PCN was achieved at pH 6, reaching $1.99 \text{ mmol g}_{\text{cat}}^{-1} \text{ h}^{-1}$. This performance is also superior to that of the most recent reports in terms of pure water system (Table S3). Moreover, the apparent quantum yield (Φ_{AQY}) of PCN at 420 nm for H₂O₂ synthesis was calculated (see details in Supporting Information), which was determined to be 8.7 % and 14.9 % at pH 9 and pH 6, respectively. The Φ_{AQY} of 8.7 % at pH 9 is higher than previous reports in terms of fair reaction condition (e.g. visible-light irradiation, without sacrificial agent) (Table S2), while the Φ_{AQY} of 14.9 % at pH 6 is also comparable to other photocatalysts [32]. Therefore, the PCN could be considered a high-efficiency photocatalyst, especially considering alkaline H₂O₂ synthesis.

The catalyst optical parameters, reactor optical thickness and total rate of photon absorption were also considered (see details in Supporting Information). The absorption and scattering coefficients (κ_λ and σ_λ) were determined using an experimental method reported by Satuf et al. [52]. The radiative transfer equation (RTE) and Henyey and Greenstein phase function were used in the calculation process as previous reports [53,54]. The optical properties of catalyst were summarized in Table S4. The apparent optical thickness τ_{app} for CN and PCN are calculated to be 2.1 and 0.5, respectively. With the determination of the above parameters, the total rate of photon absorption (TRPA/A) can be calculated. According to the analysis of TRPA and boundary layer of photon absorption by Acosta-Herazo et al., the most efficient rate of radiation absorption in solar powered planar reactors occurs at $\tau_{\text{app}} = 4.1-4.4$. In comparison, the τ_{app} for the reactor in this work is much smaller (0.5 for

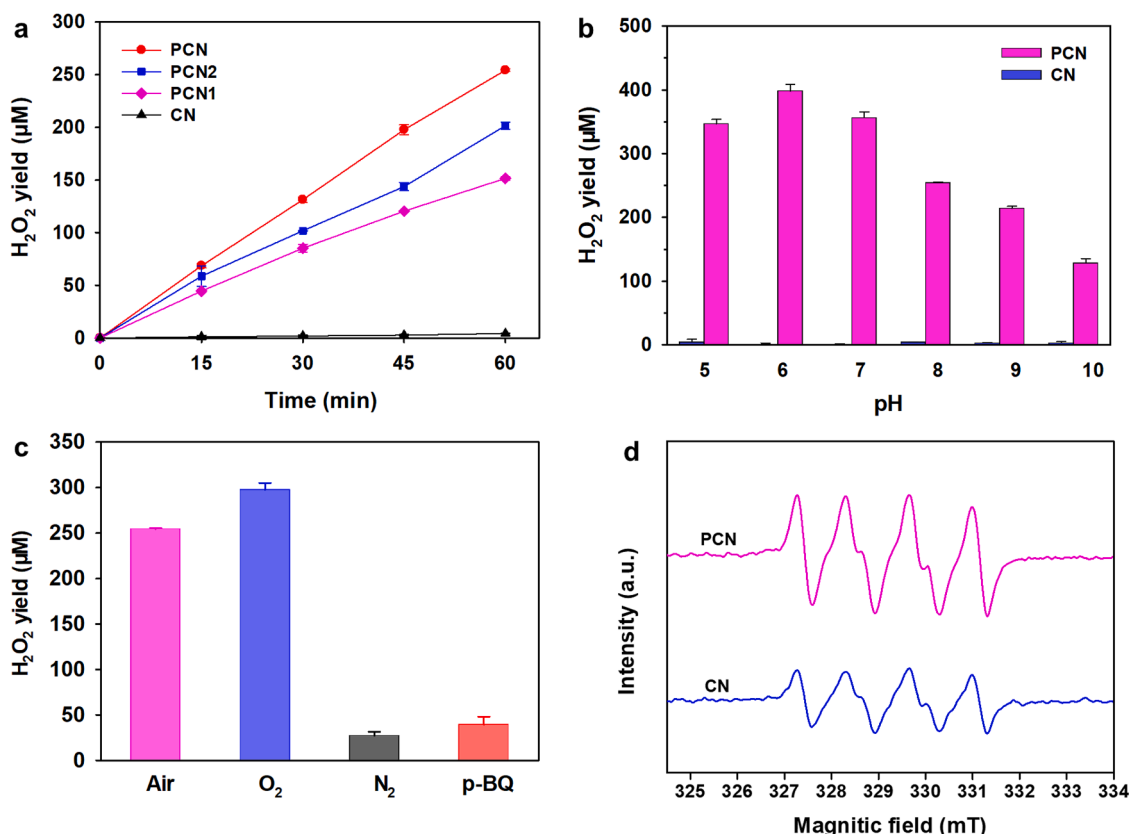


Fig. 3. (a) Photocatalytic H₂O₂ generation on CN and PCN at pH 8 under visible-light irradiation. (b) The H₂O₂ yield at different pH values for CN and PCN after 1-hour photoreaction. (c) The 1-hour H₂O₂ yield for PCN under different solution conditions. (d) Electron paramagnetic resonance (EPR) spectra of ·O₂-DMPO adduct for CN and PCN under visible-light irradiation for 5 min.

PCN), which should be due to the use of a low concentration of catalyst suspension. To make the best of solar energy, a higher concentration of catalyst suspension could be adopted to improve the TRPA. The performance of CN and PCN on H₂O₂ generation was also compared by controlling the “optical thickness” at an equal value. It was found that the CN still exhibits a much lower performance than that of PCN (Fig. S8a), indicating the superior photocatalytic activity of PCN to CN. To examine the potential pH effect on the catalyst optical thickness, the τ_{app} of PCN at different pH values was determined. The results show that the τ_{app} for PCN suspension at pH 7, 8, 9, and 10 are 0.51, 0.45, 0.52, and 0.50, respectively. Therefore, the optical thickness of PCN at different pH is basically stable.

We further conducted experiments to obtain mechanistic insights to the pathway for H₂O₂ generation. It was found that the H₂O₂ yield increases by 17 % under O₂-saturated condition, and greatly inhibited by 90 % once removing dissolved O₂ with N₂-bubbling (Fig. 3c). This proves the H₂O₂ generation on PCN via ORR dominantly. The incomplete inhibition of H₂O₂ generation in N₂-saturated condition should be associated with the h⁺-induced water oxidation process. Actually, the h⁺ of g-C₃N₄-based photocatalysts is known for water oxidation, leading to generation of O₂ and/or H₂O₂ directly [55,56]. The two ORR pathways for H₂O₂ generation, including the stepwise reduction (Eqs. 1–2) and one-step reduction (Eq. 3) processes, can be distinguished by detection and quenching of the key intermediate, superoxide anion (·O₂⁻) [32]. By adding p-benzoquinone (p-BQ) to quench ·O₂⁻, remarkable inhibiting effect on H₂O₂ generation was observed (Fig. 3c), indicating the role of ·O₂⁻ as the key intermediate of H₂O₂. EPR spectra for detection of ·O₂⁻ were recorded by using 5,5-dimethyl-1-pyrroline-N-oxide (DMPO) as a spin trap and under visible-light irradiation. As shown in Fig. 3d, a four-line signal with an intensity ratio of 1:1:1:1 was observed for both CN and PCN, corresponding well with the spectra of the ·O₂⁻-DMPO

adduct [32]. This result strongly proves the generation of ·O₂⁻. Therefore, the stepwise reduction of O₂ should be the predominant pathway for production of H₂O₂ on both CN and PCN. Furthermore, the signal intensity of ·O₂⁻ for PCN is much stronger compared with CN, suggesting the more efficient ORR on PCN.

The reusability of PCN was evaluated according to the performance in cycling experiments. The H₂O₂ yield has no significant decrease (< 8 %) after 5 times of cycling test, suggesting the good reusability of PCN for the production of H₂O₂ under visible light (Fig. S9). Moreover, FT-IR spectra of PCN before and after photo-irradiation was compared to show its stability. It was found that the signals associated with the C-N heterocyclic structure of g-C₃N₄ remains after photoreaction, including the triazine units, C-N, C=N, and cyano groups (Fig. S10). These results demonstrate the good reusability and stability of the PCN as photocatalyst.

The role of holes (h⁺) in the photocatalytic process is further studied. The water oxidation by PCN was examined by recording the linear sweep voltammetry (LSV) curves of catalyst loaded on a FTO electrode. As shown in Fig. S11, distinct positive current representing water oxidation process can be observed, and a larger current density is observed for PCN. The g-C₃N₄-based photocatalysts are well-known for water splitting to generate H₂ and O₂ [57]. As the O₂ generated through water oxidation in photocatalytic process is easy to be reduced to H₂O₂, it is hard to detect O₂ directly. However, the photocatalytic H₂O₂ generation in N₂-saturated condition (27.3 μM after 1-hr irradiation, Fig. 3c) could reflect the generation of O₂ via water oxidation. These results suggest the occurrence of h⁺-induced water oxidation.

3.4. Mechanism for efficient alkaline H₂O₂ generation

In consideration of the reaction pathway, the alkaline H₂O₂

generation requires the photocatalyst favorable for 1) proton shuttle to provide protons as reactant, and 2) O_2 adsorption and activation. Given the efficient alkaline H_2O_2 generation on PCN, we examined these aspects for PCN by experiments and theoretical calculations. First of all, the proton shuttle capacity of PCN was examined. The suspension pH of catalysts in various concentrations were measured. It was found that the suspension containing different concentrations of CN is weak acidic (pH ~ 5.6) (Fig. 4a). On the contrary, the suspension of PCN is alkaline ($9.6 < \text{pH} < 10.4$), and the pH values exhibit an increase trend with increasing concentrations of PCN. Moreover, the suspension pH for g- C_3N_4 incorporated with different amount of pyrophosphate also shows an increase trend, namely PCN1 (pH 9.5) < PCN2 (pH 10.0) < PCN (pH 10.2). This observation indicates that PCN has a stronger ability than CN to adsorb protons from water by promoting the dissociation of water.

Furthermore, the proton donating capacity was evaluated by the increase of suspension pH with addition of potassium hydroxide (KOH) to monitor the consumption of protons. As shown in Fig. 4b, the KOH-induced pH increase for PCN is much more moderate compared with CN. When adding 0.05 and 0.1 mM KOH, the pH increase for suspension of PCN is within 0.2–0.6, while it reaches 1.0–1.6 for CN, indicating the superior proton donating capacity of PCN. To further demonstrate the proton shuttle property of PCN, polarization curves were recorded in Ar-saturated condition. As shown in Fig. 4c, the negative current density represents the occurrence of hydrogen evolution reaction (HER). It was found that the current density for PCN is much larger than that of CN, which should be attributed to a faster mass transfer of protons at the interface of PCN [58]. These results demonstrate the proton shuttle property of PCN, which is beneficial to make more protons available for alkaline H_2O_2 generation.

Secondly, the adsorption and activation of O_2 molecules on PCN were investigated. The O_2 adsorption capacity of catalysts was investigated by temperature programmed desorption (TPD) measurements. The signal intensity of thermal conductivity detector (TCD) can reflect the amount of pre-adsorbed O_2 on materials. A broad signal at $\sim 160^\circ\text{C}$ was observed for CN, corresponding to the weak physical adsorption of O_2 (Fig. S12). While for PCN, the signal is stronger and shifts to a higher temperature ($\sim 220^\circ\text{C}$), which can be attributed to the stronger interaction between O_2 and PCN [59]. Moreover, the signal intensity for PCN is larger than that for CN, suggesting the higher O_2 adsorption affinity. The activation process of O_2 on CN and PCN were further studied by density functional calculation. Fig. 5a presents the interaction between O_2 and CN. After structure relaxation, the O_2 is far away from the g- C_3N_4 substrate, and O-O bond is not elongated. Moreover, the adsorption energy (E_{ads}) is calculated according to Eq. 6. It was found that the E_{ads} is only -0.05 eV . These results suggest the weak interaction between CN and O_2 . Consequently, the adsorption of O_2 on CN is unfavorable, thus, limiting the ORR for H_2O_2 generation.

$$E_{\text{ads}} = E_{\text{tot}} - E_{\text{substrate}} - E_{O_2} \quad (6)$$

where E_{ads} is the adsorption energy, E_{tot} is the total energy of the

molecule on the substrate, $E_{\text{substrate}}$ is the energy of the substrate, E_{O_2} is the energy of the O_2 adsorbed.

When pyrophosphate is introduced into the g- C_3N_4 , significant difference occurs. Here, to fully study the possible sites for the O_2 activation on PCN. Five possible sites were investigated as shown in Fig. 5b-f. It was observed that O_2 can only be activated at site 1. There is no obvious interaction between O_2 and PCN for site 2–4, and the O_2 tends to leave the surfaces of PCN after structure relaxation. In this model, the pyrophosphate acts as the key active sites for O_2 activation, and the two O atoms of O_2 are limited around one $[P-O]^-$ group and another P atom of pyrophosphate, respectively. This means that the O_2 would compete the sites of $[P-O]^-$ with protons, which could explain the decreased H_2O_2 yield from pH 6 to pH 5. There are different existing forms for pyrophosphate at acidic or alkaline conditions, namely the transformation between $(P-O)^-$ and $(P-OH)$. In an acidic condition (i.e. pH 5), the $(P-O)^-$ groups of pyrophosphate are readily to accept H^+ to form $(P-OH)$. Consequently, the oxygen reduction process would be limited as only the anion form of $(P-O)^-$ could be effective active sites for O_2 adsorption and activation. This would lead to the decrease of H_2O_2 yield even in a more acidic condition, because proton is no more the rate-determining step for H_2O_2 synthesis.

Specifically, for site 1 at the initial state (before relaxation), a P_2O_7 unit is located on the top of the C_3N_4 substrate (Fig. 5b). The O-O bond of O_2 is about 1.21 \AA [32]. After structure relaxation, the system reaches the lowest energy state (Fig. 5b). It can be found that the P_2O_7 interacts with the C_3N_4 substrate by forming a C-O bond with a length of about 1.47 \AA , and the calculated interaction energy between P_2O_7 and C_3N_4 is -3.32 eV . These results are in good agreement with the characterization results of PCN that pyrophosphate is incorporated to g- C_3N_4 via C-O bonding. Importantly, the P_2O_7 - C_3N_4 system is beneficial for the O_2 activation process. The O-O bond length of the O_2 molecule increases remarkably from 1.21 \AA to 1.44 \AA , and the two O atoms from the O_2 interact with one O atom and one P atom from the P_2O_7 unit. The E_{ads} for O_2 on the P_2O_7 - C_3N_4 is calculated to be about -4.11 eV . The negative value strongly indicates that the activation of O_2 is thermodynamically favorable.

Based on above analysis, the alkaline H_2O_2 generation on PCN via O_2 reduction can be illustrated as Fig. 6. First of all, the O_2 molecule is adsorbed by the pyrophosphate and limited around the $(P-O)^-$ group. Then, the O_2 obtains an e^- from the electron-rich $[P-O]^-$ group and gets reduced to form $\cdot O_2^-$, which tends to bind with a proton from the nearby $[P-OH]$ groups. Afterwards, the $[P-O]^-$ would be protonated again by inducing the water dissociation. The $\cdot O_2H$ is further reduced to O_2H^- by photo-generated e^- , and would be released by the $[P-O]^-$ group. Finally, the $[P-OH]$ provides another proton to bind with O_2H^- , leading to generation of H_2O_2 . The protonation of $[P-O]^-$ would enable the occurrence of next cycle for O_2 reduction.

Thirdly, the e^- donating property of catalysts for ORR was investigated by a series of photo-electrochemical measurements. Fig. 7a shows the time-resolved transient photoluminescence (PL) decay curves, which

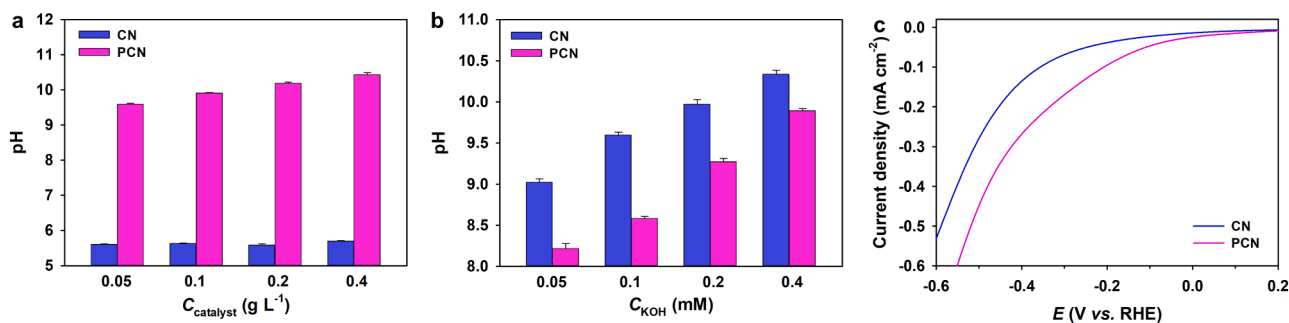


Fig. 4. (a) The pH values of suspension of CN and PCN in different concentrations. (b) The pH value of suspension of CN and PCN (initially at pH 8) with addition of different concentrations of KOH. (c) The HER polarization curves of CN and PCN with a scan rate of 5 mV s^{-1} , without iR compensation.

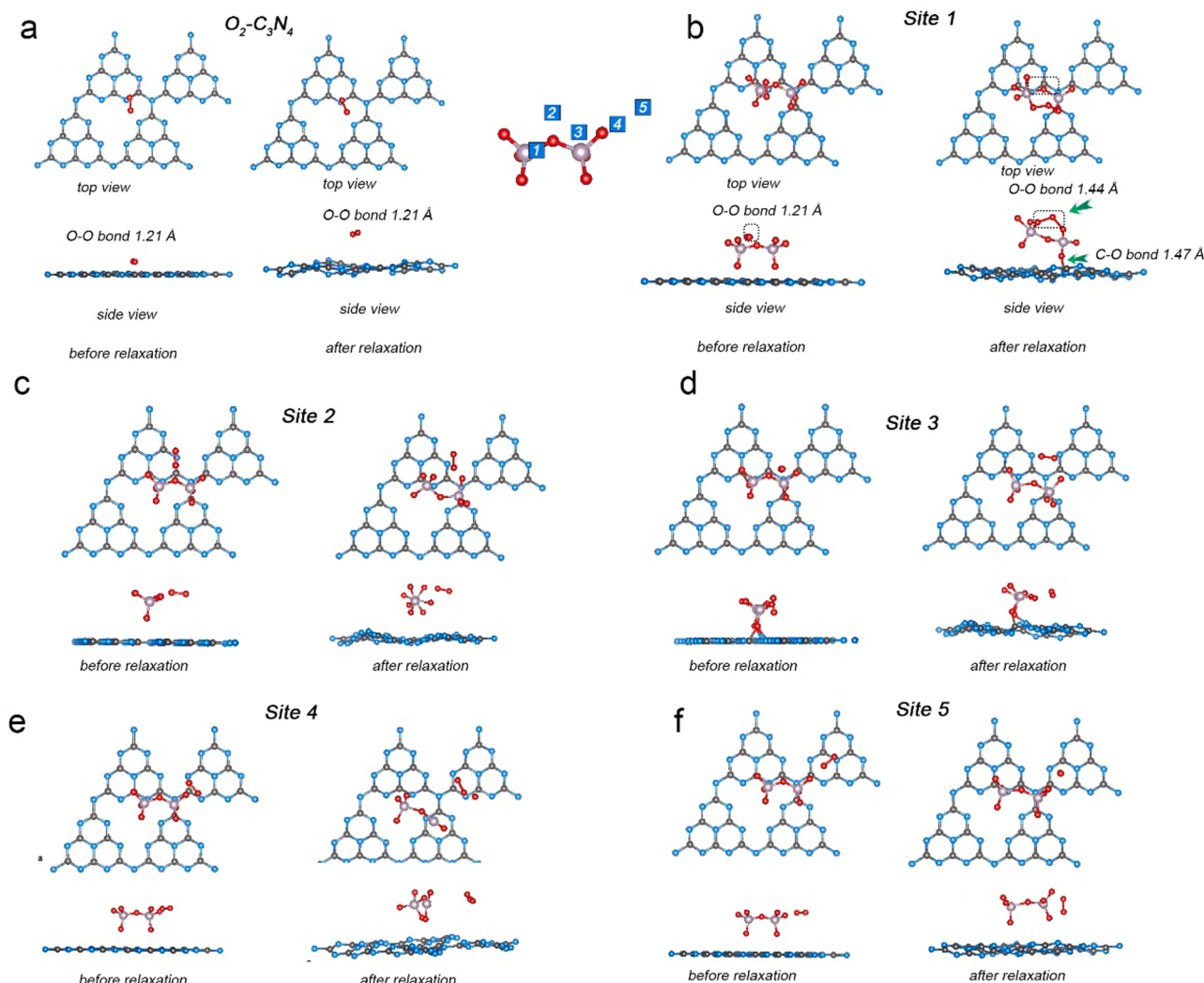


Fig. 5. Activation process of O_2 on (a) CN and (b-e) PCN for 5 possible sites.

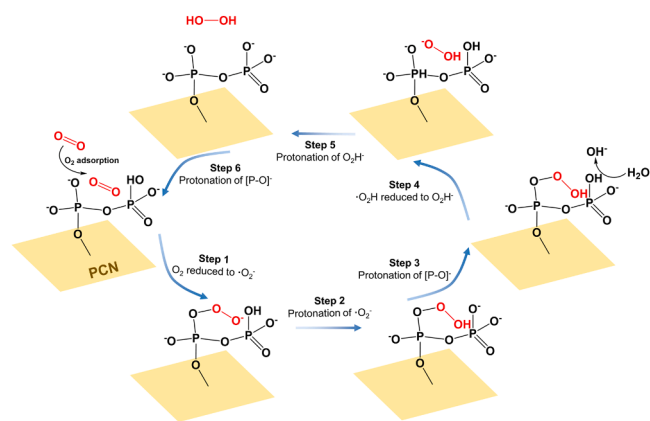


Fig. 6. Schematic diagram for the O_2 reduction process on PCN for H_2O_2 generation.

can be fitted with a multiple-exponential function. Results show that the fast decay components (τ_1) are 0.93 and 2.60 ns for CN and PCN. The greatly increased τ_1 for PCN indicates the slower recombination of interband exciton, thus, enabling more e^- available for ORR [60]. Moreover, the steady-state PL intensity for PCN is weaker than that of CN (Fig. 7b), as well as the catalysts with less pyrophosphate contents

(PCN1 and PCN2) (Fig. S13a). These results suggest the role of pyrophosphate to suppress the recombination of photo-generated charge carries. According to the I-T curves in Fig. 7c, the photocurrent density for PCN is 2.4 times higher than that of CN, and an increase trend was observed with the increased content of pyrophosphate (Fig. S13b). This result suggests the improved charge carrier separation due to the presence of pyrophosphate. The electrochemical impedance spectroscopies (EIS) were shown in Fig. 7d. The decreased semicircle for PCN suggests the lower electric resistance compared with CN, which is beneficial for the transfer of e^- to the surfaces of catalyst for reduction reactions. The significantly improved properties of PCN on charge separation and transfer should be also the key to efficient alkaline H_2O_2 production.

3.5. On-site organic pollutant treatment

H_2O_2 is an effective oxidant for treatment of aqueous refractory organic pollutants through activation to generate hydroxyl radicals ($\cdot OH$). Photocatalysis is a green and sustainable approach widely used to convert H_2O_2 into $\cdot OH$ [20,21]. Taking this advantage, the H_2O_2 generation and in-situ activation occur simultaneously in photocatalytic process. This could be a sustainable and convenient approach for on-site treatment of pollutants. Here, we investigated the degradation of three kinds of typical organic pollutants by PCN photocatalyst, including dyes (i.e. Rhodamine B), antibiotics (i.e. ofloxacin), and endocrine-disrupting chemicals (EDCs, i.e. bisphenol A). These pollutants are commonly

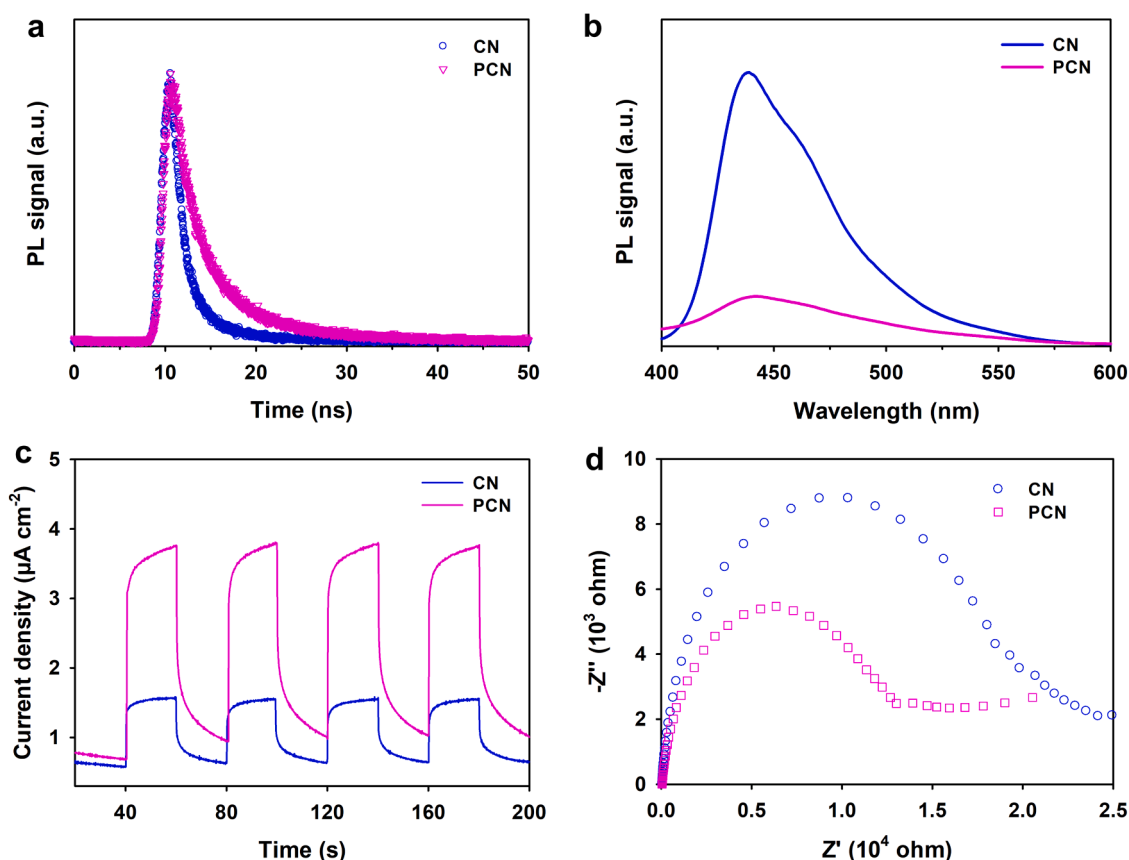


Fig. 7. (a) Time-resolved photoluminescence spectra, (b) Steady-state photoluminescence spectra, (c) Photocurrent responses, and (d) Nyquist plots of CN and PCN.

found but difficult to degrade in alkaline wastewater and nature water, and the treatment of them in alkaline conditions has drew increasing attention because of their acute or chronic toxicity to human and aquatic organisms [61–65].

Fig. 8a shows the performance of CN and PCN for pollutant degradation in alkaline water. The PCN could rapidly degrade all the three kinds of pollutants, which is much more efficient compared with CN. For example, the removal efficiency of OFL at 15 min is more than 98 % for PCN, while it is only 25 % for CN; and the degradation rate of BPA on PCN (2.0 h^{-1}) is 4.7 times higher than that on CN (0.43 h^{-1}). Moreover, at an equal value of “optical thickness”, the PCN still exhibits a much higher performance than that of CN (Fig. S8b), indicating the superior activity of PCN. The performance of CN and PCN in a series of pH values (pH 5 to pH 10) were further evaluated by BPA degradation. As shown in Fig. 8b, the BPA removal efficiency for PCN is much higher than that for CN at all of the pH values (pH 5–10). The degradation rate of BPA for PCN is 5.5–11.8 times higher than that for CN (Fig. 8c), demonstrating the superior efficiency of PCN to CN for treatment of organic pollutants. With the pH increase (from pH 5 to pH 10), the degradation rate of BPA gradually decreases, which should be ascribed to the decreased H_2O_2 generation in more alkaline conditions (Fig. 3b). However, considering the moderate decrease of removal efficiency of BPA (from 93 % to 83 %), the PCN can still be considered as a high-efficiency photocatalyst for degradation of BPA even in alkaline conditions.

The mechanism for BPA degradation on PCN was studied by quenching experiments. As mentioned above, the BPA degradation is associated with the H_2O_2 generation rate. Therefore, the BPA degradation should be induced by H_2O_2 and/or its derivative, $\cdot\text{OH}$. Hence, isopropanol (IPA) was involved as the scavenger of $\cdot\text{OH}$ [66]. It was found that the degradation of BPA was significantly inhibited by IPA in all tested pH values (5–10) (Fig. S14a). The degradation rate of BPA was decreased by 65–77 % (Fig. S14b), indicating the key role of $\cdot\text{OH}$ for BPA

degradation. The generation of $\cdot\text{OH}$ was characterized by EPR measurements. As displayed in Fig. 8d, typical EPR spectra of the $\cdot\text{OH}$ -DMPO adduct (four-line signal with an intensity ratio of 1:2:2:1) was observed for both CN and PCN [67]. Moreover, the signal of $\cdot\text{OH}$ for PCN is much stronger than that of CN, indicating the efficient $\cdot\text{OH}$ generation. Accordingly, the PCN could exhibit superior activity to CN for $\cdot\text{OH}$ -mediated environmental treatment.

In addition, the role of other oxidative species was also evaluated, including photo-generated h^+ and singlet oxygen ($^1\text{O}_2$), which has been also reported to degrade BPA [35,68]. Oxalate and furfuryl alcohol (FFA) were used as the scavenger of h^+ and singlet oxygen, respectively [35]. As shown in Fig. S15, the BPA degradation rate only decreased by 21 % in presence of oxalate, suggesting the minor role of h^+ . Due to the oxidation of BPA by h^+ , the H_2O_2 generation is slightly enhanced (Fig. S16). This is because the consumption of h^+ by BPA could promote the separation efficiency of h^+/e^- pairs and allowing more e^- available for oxygen reduction to form H_2O_2 . Moreover, the inhibiting effect of furfuryl alcohol (FFA) on BPA degradation is quite limited (Fig. S15). These observations together with the remarkable inhibiting effect of IPA proves the major role of $\cdot\text{OH}$ for BPA degradation.

Total organic carbon (TOC) and liquid chromatography-mass (LC-MS) measurements were conducted to investigate the mineralization of organic pollutants and their intermediates in the degradation process, respectively. As shown in Fig. S17, significant decrease of TOC was found for both the three kinds of pollutants (i.e. BPA, RhB, and OFL) during the photocatalysis of PCN, especially for BPA (40 % decrease in 4 h). This indicates the effective mineralization of organic pollutants on PCN. BPA was used as a typical pollutant to study the degradation pathway. The total ion current (TIC) of chromatograms of the reaction solutions of BPA after 2-hr irradiation is shown in Fig. S18. Several new peaks could be observed, and the ion mass spectra are presented in Fig. S19. The peak at m/z 265 corresponds to BPA [(M-K) $^+$], and the

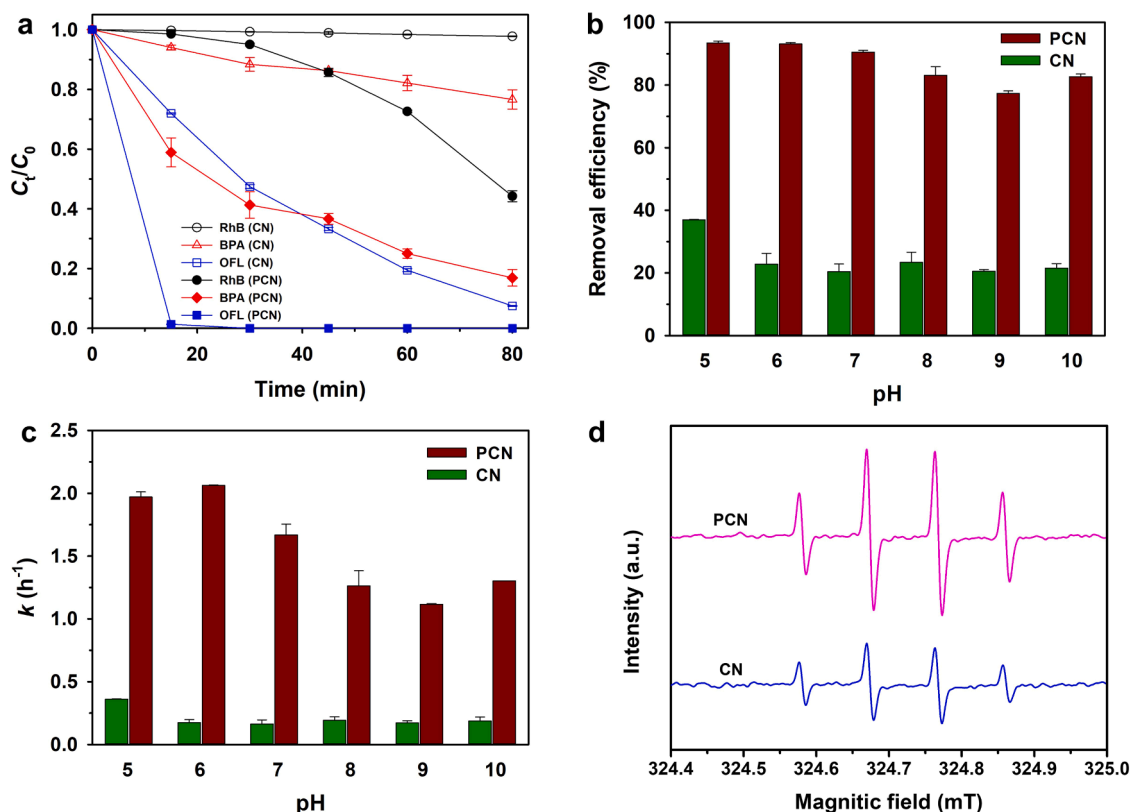


Fig. 8. (a) Photocatalytic degradation of ofloxacin (OFL), bisphenol A (BPA), and Rhodamine B (RhB) on CN and PCN (0.2 g/L) at pH 8 under visible light. (b) Photocatalytic removal efficiency of BPA on CN and PCN at different pH values. (c) The pseudo-first-order rates for BPA degradation on CN and PCN at different pH values. (d) EPR spectra of $\cdot\text{OH}$ -DMPO adduct for CN and PCN under visible-light irradiation for 5 min.

other peaks at m/z 319 [(M-2 K) $^+$], 135 [(M-H) $^+$], and 122 [(M-H) $^+$], are stemmed from BPA degradation typically due to $\cdot\text{OH}$ attack [69,70]. Based on these results, the pathways for BPA degradation are proposed in Fig. S20.

The toxicity of BPA and its degradation intermediates were compared based on previous toxicologic studies. The first-step degradation intermediates of BPA mainly includes 4-isopropylphenol and monohydroxylated BPA. The 96-hr EC50 of 4-isopropylphenol and monohydroxylated BPA for green algae are 38 and 13.3 mg/L, which is significantly higher than that of BPA itself (2.7 mg/L) [71–73]. This indicates the elimination of toxicity of BPA induced by the photocatalytic degradation. Moreover, with a longer time for photocatalytic degradation, the final intermediates would mainly composed of small carboxylic acids/alcohols with lower toxicity, and they are also very prone to mineralization. Hence, the degradation of BPA using PCN photocatalyst could be considered a process to reduce and finally eliminate the toxicity of BPA.

4. Conclusions

Efficient on-site H_2O_2 synthesis in alkaline water remains a challenge for current methods. In this work, a novel pyrophosphate-based proton shuttle strategy was proposed to boost alkaline photocatalytic H_2O_2 generation. The pyrophosphate on PCN could serve as proton shuttle to effectively provide protons for alkaline H_2O_2 generation, and the [P-O] $^-$ was found to be active sites for O_2 adsorption and activation. Moreover, the incorporation of pyrophosphate tunes the band structure of PCN and facilitate the charge separation and transfer. As a result, efficient H_2O_2 production in neutral to alkaline water (e.g. $1071.7 \mu\text{mol g}_{\text{cat}}^{-1} \text{h}^{-1}$ at pH 9) has been achieved. Taking this advantage, efficient degradation of various organic pollutants in alkaline water has been achieved due to the in-situ activation of H_2O_2 product to form $\cdot\text{OH}$. Therefore, the PCN with

superior H_2O_2 synthesis efficiency could obtain promising environmental applications, especially for on-site treatment of alkaline water.

CRediT authorship contribution statement

Liangpang Xu: Methodology, Conceptualization, Software, Investigation, Resources, Data curation, Writing-original draft. Lejing Li: Formal analysis, Investigation, Resources. Zhuofeng Hu: Conceptualization, Methodology, Formal analysis, Data curation, Writing-review & editing, Funding acquisition. Jimmy C. Yu: Conceptualization, Writing-review & editing, Supervision, Funding acquisition.

Declaration of Competing Interest

The authors declare that they have no known competing financial interests or personal relationships that could have appeared to influence the work reported in this paper.

Data Availability

Data will be made available on request.

Acknowledgements

This work is supported by the financial support from the Research Grants Council of Hong Kong, Hong Kong (Project 14304019), the National Natural Science Foundation of China (Grant No. 51902357), the Guangzhou Basic and Applied Basic Research Foundation, China (202201011695), the Fundamental Research Funds for the Central Universities, Sun Yat-sen University (22lgqb23), and the Science and Technology Planning Project of Guangdong Province (2020A0505100032). The theoretical calculation is supported by

National Supercomputer Center in Guangzhou and National Supercomputing Center in Shenzhen (Shenzhen Cloud Computing Center).

References

- [1] D.B. Miklos, C. Remy, M. Jekel, K.G. Linden, J.E. Drewes, U. Hübner, Evaluation of advanced oxidation processes for water and wastewater treatment—a critical review, *Water Res.* 139 (2018) 118–131.
- [2] M. Pera-Titus, V. García-Molina, M.A. Baños, J. Giménez, S. Esplugas, Degradation of chlorophenols by means of advanced oxidation processes: a general review, *Appl. Catal. B* 47 (2004) 219–256.
- [3] J. Fierro, J.M. Campos-martin, G. Blanco-brieva, Hydrogen peroxide synthesis: an outlook beyond the anthraquinone process angewandte, *Angew. Chem. Int. Ed.* 45 (2006) 6962–6984.
- [4] Y. Yang, G. Zeng, D. Huang, C. Zhang, D. He, C. Zhou, W. Wang, W. Xiong, X. Li, B. Li, Molecular engineering of polymeric carbon nitride for highly efficient photocatalytic oxytetracycline degradation and H₂O₂ production, *Appl. Catal. B* 272 (2020), 118970.
- [5] P. Zhang, Y. Tong, Y. Liu, J.J.M. Vequizo, H. Sun, C. Yang, A. Yamakata, F. Fan, W. Lin, X. Wang, Heteroatom dopants promote two-electron O₂ reduction for photocatalytic production of H₂O₂ on polymeric carbon nitride, *Angew. Chem. Int. Ed.* 132 (2020) 16343–16351.
- [6] Y. Mu, Y. Chen, Q. Fu, P.-Y. He, Q. Sun, J.-P. Zou, L. Zhang, D. Wang, S. Luo, Transformation of atrazine to hydroxyatrazine with alkali-H₂O₂ treatment: an efficient dechlorination strategy under alkaline conditions, *ACS EST Water* 1 (2021) 1868–1877.
- [7] L. Li, Z. Hu, J.C. Yu, On-demand synthesis of H₂O₂ by water oxidation for sustainable resource production and organic pollutant degradation, *Angew. Chem. Int. Ed.* 132 (2020) 20719–20725.
- [8] C. Xu, D. Hinks, A. El-Shafei, P. Hauser, M. Li, M. Ankeny, K. Lee, Review of bleach activators for environmentally efficient bleaching of textiles, *J. Fiber Bioeng. Inform.* 4 (2011) 209–219.
- [9] S.C. Perry, D. Pangotra, L. Vieira, L.-I. Csepei, V. Sieber, L. Wang, C. Ponce de León, F.C. Walsh, Electrochemical synthesis of hydrogen peroxide from water and oxygen, *Nat. Rev. Chem.* 3 (2019) 442–458.
- [10] H. Hou, X. Zeng, X. Zhang, Production of hydrogen peroxide by photocatalytic processes, *Angew. Chem. Int. Ed.* 59 (2020) 17356–17376.
- [11] C. Feng, L. Tang, Y. Deng, J. Wang, J. Luo, Y. Liu, X. Ouyang, H. Yang, J. Yu, J. Wang, Synthesis of leaf-vein-like g-C₃N₄ with tunable band structures and charge transfer properties for selective photocatalytic H₂O₂ evolution, *Adv. Funct. Mater.* 30 (2020), 2001922.
- [12] Q. Hu, Y. Dong, K. Ma, X. Meng, Y. Ding, Amidation crosslinking of polymeric carbon nitride for boosting photocatalytic hydrogen peroxide production, *J. Catal.* 413 (2022) 321–330.
- [13] C. Feng, L. Tang, Y. Deng, J. Wang, J. Luo, Y. Liu, X. Ouyang, H. Yang, J. Yu, J. Wang, Synthesis of leaf-vein-like g-C₃N₄ with tunable band structures and charge transfer properties for selective photocatalytic H₂O₂ evolution, *Adv. Funct. Mater.* 30 (2020), 2001922.
- [14] Z. Teng, Q. Zhang, H. Yang, K. Kato, W. Yang, Y.-R. Lu, S. Liu, C. Wang, A. Yamakata, C. Su, Atomically dispersed antimony on carbon nitride for the artificial photosynthesis of hydrogen peroxide, *Nat. Catal.* 4 (2021) 374–384.
- [15] M. Kou, Y. Wang, Y. Xu, L. Ye, Y. Huang, B. Jia, H. Li, J. Ren, Y. Deng, J. Chen, Molecularly engineered covalent organic frameworks for hydrogen peroxide photosynthesis, *Angew. Chem. Int. Ed.* 61 (2022), e202200413.
- [16] Y. Wang, J. Zhao, W. Hou, Y. Xu, Decoration of CdS nanowires with Ni₃S₄ nanoballs enhancing H₂ and H₂O₂ production under visible light, *Appl. Catal. B* 310 (2022), 121350.
- [17] Z.-L. Zhou, Y.-T. Xiao, J. Tian, N. Nan, R.-J. Song, J.-H. Li, Recent advances in metal-free covalent organic frameworks for photocatalytic applications in energy and environment, *J. Mater. Chem.*, (2023).
- [18] W. Lee, H.J. Son, D.-K. Lee, B. Kim, H. Kim, K. Kim, M.J. Ko, Suppression of photocorrosion in CdS/CdSe quantum dot-sensitized solar cells: Formation of a thin polymer layer on the photoelectrode surface, *Synth. Met.* 165 (2013) 60–63.
- [19] S. Zhang, X. Ou, Q. Xiang, S.A. Carabineiro, J. Fan, K. Lv, Research progress in metal sulfides for photocatalysis: From activity to stability, *Chemosphere* (2022), 135085.
- [20] Y. Cui, Z. Ding, P. Liu, M. Antonietti, X. Fu, X. Wang, Metal-free activation of H₂O₂ by g-C₃N₄ under visible light irradiation for the degradation of organic pollutants, *Phys. Chem. Chem. Phys.* 14 (2012) 1455–1462.
- [21] C.S. Zalazar, M.L. Satuf, O.M. Alfano, A.E. Cassano, Comparison of H₂O₂/UV and heterogeneous photocatalytic processes for the degradation of dichloroacetic acid in water, *Environ. Sci. Technol.* 42 (2008) 6198–6204.
- [22] C. Chu, W. Miao, Q. Li, D. Wang, Y. Liu, S. Mao, Highly efficient photocatalytic H₂O₂ production with cyano and SnO₂ co-modified g-C₃N₄, *Chem. Eng. J.* 428 (2022), 132531.
- [23] H. Zhuang, L. Yang, J. Xu, F. Li, Z. Zhang, H. Lin, J. Long, X. Wang, Robust photocatalytic H₂O₂ production by octahedral Cd₃(C₃N₃S₃)₂ coordination polymer under visible light, *Sci. Rep.* 5 (2015) 1–8.
- [24] H. Shi, Y. Li, X. Wang, H. Yu, J. Yu, Selective modification of ultra-thin g-C₃N₄ nanosheets on the (110) facet of Au/BiVO₄ for boosting photocatalytic H₂O₂ production, *Appl. Catal. B* 297 (2021), 120414.
- [25] Y. Jiao, Y. Zheng, M. Jaroniec, S.Z. Qiao, Design of electrocatalysts for oxygen-and hydrogen-involving energy conversion reactions, *Chem. Soc. Rev.* 44 (2015) 2060–2086.
- [26] Z. Li, Y. Feng, Y.L. Liang, C.Q. Cheng, C.K. Dong, H. Liu, X.W. Du, Stable rhodium (IV) oxide for alkaline hydrogen evolution reaction, *Adv. Mater.* 32 (2020), 1908521.
- [27] X. Xiong, X. Zhang, S. Liu, J. Zhao, Y. Xu, Sustained production of H₂O₂ in alkaline water solution using borate and phosphate-modified Au/TiC₂ photocatalysts, *Photochem. Photobiol. Sci.* 17 (2018) 1018–1022.
- [28] S. Wang, B. Cai, H. Tian, Efficient generation of hydrogen peroxide and formate by an organic polymer dots photocatalyst in alkaline conditions, *Angew. Chem. Int. Ed.* (2022), e202202733.
- [29] Y. Zhou, G.G. Hou, Effects of phosphate salts on the pH values and rapid visco analyser (RVA) pasting parameters of wheat flour suspensions, *Cereal Chem.* 89 (2012) 38–43.
- [30] D.J. Scott, M.J. Fuchter, A.E. Ashley, Designing effective ‘frustrated Lewis pair’hydrogenation catalysts, *Chem. Soc. Rev.* 46 (2017) 5689–5700.
- [31] M. Huang, S. Gong, C. Wang, Y. Yang, P. Jiang, P. Wang, L. Hu, Q. Chen, Lewis-Basic EDTA as a highly active molecular electrocatalyst for CO₂ reduction to CH₄, in: *Angew. Chem. Int. Ed.*, 133, 2021, pp. 23184–23191.
- [32] L. Xu, Y. Liu, L. Li, Z. Hu, J.C. Yu, Fabrication of a photocatalyst with biomass waste for H₂O₂ synthesis, *ACS Catal.* 11 (2021) 14480–14488.
- [33] Z.-A. Lan, G. Zhang, X. Wang, A facile synthesis of Br-modified g-C₃N₄ semiconductors for photoredox water splitting, *Appl. Catal. B* 192 (2016) 116–125.
- [34] B. Liu, J. Du, G. Ke, B. Jia, Y. Huang, H. He, Y. Zhou, Z. Zou, Boosting O₂ reduction and H₂O dehydrogenation kinetics: surface N-hydroxymethylation of g-C₃N₄ photocatalysts for the efficient production of H₂O₂, *Adv. Funct. Mater.* 32 (2022), 2111125.
- [35] L. Xu, L. Li, L. Yu, J.C. Yu, Efficient generation of singlet oxygen on modified g-C₃N₄ photocatalyst for preferential oxidation of targeted organic pollutants, *Chem. Eng. J.* 431 (2022), 134241.
- [36] Y. Zhang, S. Zong, C. Cheng, J. Shi, X. Guan, Y. Lu, L. Guo, One-pot annealing preparation of Na-doped graphitic carbon nitride from melamine and organometallic sodium salt for enhanced photocatalytic H₂ evolution, *Int. J. Hydrog. Energy* 43 (2018) 13953–13961.
- [37] W. Liu, C. Song, M. Kou, Y. Wang, Y. Deng, T. Shimada, L. Ye, Fabrication of ultra-thin g-C₃N₄ nanoplates for efficient visible-light photocatalytic H₂O₂ production via two-electron oxygen reduction, *Chem. Eng. J.* 425 (2021), 130615.
- [38] P. Shih, S. Yung, T. Chin, FTIR and XPS studies of P₂O₅-Na₂O-CuO glasses, *J. Non-Cryst. Solids* 244 (1999) 211–222.
- [39] X. Zhao, Y. Zhang, F. Li, Y. Wang, W. Pan, D.Y. Leung, Salt-air template synthesis of Na and O doped porous graphitic carbon nitride nanorods with exceptional photocatalytic H₂ evolution activity, *Carbon* 179 (2021) 42–52.
- [40] J. Fu, B. Zhu, C. Jiang, B. Cheng, W. You, J. Yu, Hierarchical porous O-doped g-C₃N₄ with enhanced photocatalytic CO₂ reduction activity, *Small* 13 (2017), 1603938.
- [41] L. Chen, C. Chen, Z. Yang, S. Li, C. Chu, B. Chen, Simultaneously tuning band structure and oxygen reduction pathway toward high-efficient photocatalytic hydrogen peroxide production using cyano-rich graphitic carbon nitride, *Adv. Funct. Mater.* 31 (2021), 2105731.
- [42] H. Yu, H. Ma, X. Wu, X. Wang, J. Fan, J. Yu, One-step realization of crystallization and cyano-group generation for g-C₃N₄ photocatalysts with improved H₂ production, *Sol. RRL* 5 (2021), 2000372.
- [43] S. Zhang, Y. Liu, P. Gu, R. Ma, T. Wen, G. Zhao, L. Li, Y. Ai, C. Hu, X. Wang, Enhanced photodegradation of toxic organic pollutants using dual-oxygen-doped porous g-C₃N₄: Mechanism exploration from both experimental and DFT studies, *Appl. Catal. B* 248 (2019) 1–10.
- [44] R.K. Brow, An XPS study of oxygen bonding in zinc phosphate and zinc borophosphate glasses, *J. Non-Cryst. Solids* 194 (1996) 267–273.
- [45] W. Fang, J. Liu, L. Yu, Z. Jiang, W. Shangqian, Novel (Na, O) co-doped g-C₃N₄ with simultaneously enhanced absorption and narrowed bandgap for highly efficient hydrogen evolution, *Appl. Catal. B* 209 (2017) 631–636.
- [46] M. Crobu, A. Rossi, F. Mangolini, N.D. Spencer, Chain-length-identification strategy in zinc polyphosphate glasses by means of XPS and ToF-SIMS, *Anal. Bioanal. Chem.* 403 (2012) 1415–1432.
- [47] Y. Yu, H. Guo, M. Pujari-Palmer, B. Stevensson, J. Grins, H. Engqvist, M. Eden, Advanced solid-state ¹H/³¹P NMR characterization of pyrophosphate-doped calcium phosphate cements for biomedical applications: The structural role of pyrophosphate, *Ceram. Int.* 45 (2019) 20642–20655.
- [48] C. Ferrara, C. Ritter, P. Mustarelli, C. Tealdi, Polymorphism in Na₂(Co/Zn)P₂O₇ and Na₂(Co/Fe)P₂O₇ pyrophosphates: a combined diffraction and ³¹P NMR study, *J. Phys. Chem. C* 126 (2021) 701–708.
- [49] J. Hu, C. Chen, H. Yang, F. Yang, J. Qu, X. Yang, W. Sun, L. Dai, C.M. Li, Tailoring well-ordered, highly crystalline carbon nitride nanoarrays via molecular engineering for efficient photosynthesis of H₂O₂, *Appl. Catal. B* 317 (2022), 121723.
- [50] J. Hu, X. Li, J. Qu, X. Yang, Y. Cai, T. Yang, F. Yang, C.M. Li, Bifunctional honeycomb hierarchical structured 3D/3D ReS₂/ZnIn₂S₄-Sv heterojunction for efficient photocatalytic H₂-evolution integrated with biomass oxidation, *Chem. Eng. J.* 453 (2023), 139957.
- [51] Z. Zhang, J.T. Yates Jr, Band bending in semiconductors: chemical and physical consequences at surfaces and interfaces, *Chem. Rev.* 112 (2012) 5520–5551.
- [52] M.L. Satuf, R.J. Brandi, A.E. Cassano, O.M. Alfano, Experimental method to evaluate the optical properties of aqueous titanium dioxide suspensions, *Ind. Eng. Chem. Res.* 44 (2005) 6643–6649.
- [53] R. Acosta-Herazo, M.A. Mueses, G.L. Puma, F. Machuca-Martinez, Impact of photocatalyst optical properties on the efficiency of solar photocatalytic reactors rationalized by the concepts of initial rate of photon absorption (IRPA)

- dimensionless boundary layer of photon absorption and apparent optical thickness, *Chem. Eng. J.* 356 (2019) 839–849.
- [54] R. Acosta-Herazo, J. Monterroza-Romero, M.Á. Mueses, F. Machuca-Martínez, G. L. Puma, Coupling the six flux absorption-scattering model to the henry-greenstein scattering phase function: evaluation and optimization of radiation absorption in solar heterogeneous photoreactors, *Chem. Eng. J.* 302 (2016) 86–96.
- [55] Z. Li, C. Kong, G. Lu, Visible photocatalytic water splitting and photocatalytic two-electron oxygen formation over Cu-and Fe-doped g-C₃N₄, *J. Phys. Chem. C* 120 (2016) 56–63.
- [56] X. Yang, L. Tian, X. Zhao, H. Tang, Q. Liu, G. Li, Interfacial optimization of g-C₃N₄-based Z-scheme heterojunction toward synergistic enhancement of solar-driven photocatalytic oxygen evolution, *Appl. Catal. B* 244 (2019) 240–249.
- [57] A. Mishra, A. Mehta, S. Basu, N.P. Shetti, K.R. Reddy, T.M. Aminabhavi, Graphitic carbon nitride (g-C₃N₄)-based metal-free photocatalysts for water splitting: a review, *Carbon* 149 (2019) 693–721.
- [58] J. Wang, L. Yang, L. Zhang, Constructed 3D hierarchical micro-flowers CoWO₄@Bi₂WO₆ Z-scheme heterojunction catalyzer: Two-channel photocatalytic H₂O₂ production and antibiotics degradation, *Chem. Eng. J.* 420 (2021), 127639.
- [59] Y. Deng, Z. Zhou, H. Zeng, R. Tang, L. Li, J. Wang, C. Feng, D. Gong, L. Tang, Y. Huang, Phosphorus and kalium co-doped g-C₃N₄ with multiple-locus synergies to degrade atrazine: Insights into the depth analysis of the generation and role of singlet oxygen, *Appl. Catal. B* (2022), 121942.
- [60] W. Wang, X. Bai, Q. Ci, L. Du, X. Ren, D.L. Phillips, Near-field drives long-lived shallow trapping of polymeric C₃N₄ for efficient photocatalytic hydrogen evolution, *Adv. Funct. Mater.* 31 (2021), 2103978.
- [61] J.R. Rochester, Bisphenol A and human health: a review of the literature, *Reprod. Toxicol.* 42 (2013) 132–155.
- [62] J.B. Carbajo, A.L. Petre, R. Rosal, S. Herrera, P. Letón, E. García-Calvo, A. R. Fernández-Alba, J.A. Perdigón-Melón, Continuous ozonation treatment of ofloxacin: Transformation products, water matrix effect and aquatic toxicity, *J. Hazard. Mater.* 292 (2015) 34–43.
- [63] J. Rochat, P. Demenge, J. Rerat, Toxicologic study of a fluorescent tracer: rhodamine B, *Toxicol. Eur. Res.* 1 (1978) 23–26.
- [64] J. Hong, N. Yuan, Y. Wang, S. Qi, Efficient degradation of Rhodamine B in microwave-H₂O₂ system at alkaline pH, *Chem. Eng. J.* 191 (2012) 364–368.
- [65] P.B. Dorn, C.-S. Chou, J.J. Gentempo, Degradation of bisphenol A in natural waters, *Chemosphere* 16 (1987) 1501–1507.
- [66] K.A. Hislop, J.R. Bolton, The photochemical generation of hydroxyl radicals in the UV-vis/ferrioxalate/H₂O₂ system, *Environ. Sci. Technol.* 33 (1999) 3119–3126.
- [67] J. He, W. Ma, J. He, J. Zhao, C.Y. Jimmy, Photooxidation of azo dye in aqueous dispersions of H₂O₂/α-FeOOH, *Appl. Catal. B* 39 (2002) 211–220.
- [68] H. Wang, Q. Li, S. Zhang, Z. Chen, W. Wang, G. Zhao, L. Zhuang, B. Hu, X. Wang, Visible-light-driven N₂-g-C₃N₄ as a highly stable and efficient photocatalyst for bisphenol A and Cr (VI) removal in binary systems, *Catal. Today* 335 (2019) 110–116.
- [69] Y. Huang, M. Kong, S. Coffin, K.H. Cochran, D.C. Westerman, D. Schlenk, S. D. Richardson, L. Lei, D.D. Dionysiou, Degradation of contaminants of emerging concern by UV/H₂O₂ for water reuse: kinetics, mechanisms, and cytotoxicity analysis, *Water Res.* 174 (2020), 115587.
- [70] D.P. Subagio, M. Srinivasan, M. Lim, T.-T. Lim, Photocatalytic degradation of bisphenol-A by nitrogen-doped TiO₂ hollow sphere in a vis-LED photoreactor, *Appl. Catal. B* 95 (2010) 414–422.
- [71] H.C. Alexander, D.C. Dill, L.W. Smith, P.D. Guiney, P. Dorn, Bisphenol A: acute aquatic toxicity, *Environ. Toxicol. Chem.* 7 (1988) 19–26.
- [72] M. Brinkmann, A.L. Schneider, K. Bluhm, S. Schiwy, G. Lehmann, B. Deutschmann, A. Müller, A. Tiehm, H. Hollert, Ecotoxicity of nitrogen, sulfur, or oxygen heterocycles and short-chained alkyl phenols commonly detected in contaminated groundwater, *Environ. Toxicol. Chem.* 38 (2019) 1343–1355.
- [73] J. Lin, Y. Hu, L. Wang, D. Liang, X. Ruan, S. Shao, M88/PS/Vis system for degradation of bisphenol A: environmental factors, degradation pathways, and toxicity evaluation, *Chem. Eng. J.* 382 (2020), 122931.